



HAL
open science

Flow Statistics in the Transitional Regime of Plane Channel Flow

Pavan V Kashyap, Yohann Duguet, Olivier Dauchot

► **To cite this version:**

Pavan V Kashyap, Yohann Duguet, Olivier Dauchot. Flow Statistics in the Transitional Regime of Plane Channel Flow. Entropy, 2020, 22 (9), pp.1001. 10.3390/e22091001 . hal-03032458

HAL Id: hal-03032458

<https://hal.science/hal-03032458>

Submitted on 30 Nov 2020

HAL is a multi-disciplinary open access archive for the deposit and dissemination of scientific research documents, whether they are published or not. The documents may come from teaching and research institutions in France or abroad, or from public or private research centers.

L'archive ouverte pluridisciplinaire **HAL**, est destinée au dépôt et à la diffusion de documents scientifiques de niveau recherche, publiés ou non, émanant des établissements d'enseignement et de recherche français ou étrangers, des laboratoires publics ou privés.

Article

Flow statistics in the transitional regime of plane channel flow

Pavan V. KASHYAP^{1,†,*}, Yohann DUGUET^{1,‡} and Olivier DAUCHOT^{2, }

¹ Affiliation 1; LIMSI-CNRS, UPR 3251, Université Paris-Saclay, 91405 Orsay, France

² Affiliation 2; Gulliver, ESPCI-CNRS, 10 Rue Vauquelin, 75005 Paris

* Correspondence: pavan.kashyap@limsi.fr

Version August 14, 2020 submitted to Entropy

Abstract: The transitional regime of plane channel flow is investigated away from the transitional point below which turbulence is not sustained, using direct numerical simulation in large domains. Statistics of laminar-turbulent spatiotemporal intermittency are reported. The geometry of the pattern is first characterized, including statistics for the angles of the laminar-turbulent stripes observed in this regime, with a comparison to experiments. High-order statistics of the local and instantaneous bulk velocity, wall shear stress and turbulent kinetic energy are then provided. The distributions of the two former quantities have non trivial shapes, characterized by a large kurtosis and/or skewness. Interestingly, we observe a strong linear correlation between their kurtosis and their skewness squared, which is usually reported at much higher Reynolds number in the fully turbulent regime.

Keywords: Transition to turbulence, spatiotemporal intermittency, channel flow

1. Introduction

Laminar and turbulent flows are two different regimes encountered for a given geometry. In many flows they are in competition from the point of view of the state space. Shear flows next to solid walls however show this surprisingly robust property that both laminar and turbulent regions coexist spatially on very long time scales, when the laminar state is locally stable. This phenomenon, called ‘laminar-turbulent intermittency’ is well known in circular pipe flow since the days of O. Reynolds [1] and has lead recently to a burst of interest, a review of which is provided in Ref. [2]. Such laminar-turbulent flows have been identified and partly characterized in Taylor-Couette flow [3,4] and in plane Couette flow [4–6]. They also have been identified in other set-ups involving curvature [7–9] or stabilising effects [10]. The transitional regimes of plane Poiseuille flow, the flow between two fixed parallel plates driven by a fixed pressure gradient, have not received as much attention although this flow is the archetype of wall-bounded turbulent flows. Whereas this flow is frequently cited as an example of flow developing a linear instability (under the form of Tollmien-Schlichting waves) [11], coherent structures typical of laminar-turbulent coexistence have been frequently reported in channel flow well below the linear instability threshold and a series of experimental and cutting-edge numerical studies in the 1980s and 1990s have focused on the development of spots [12–16]. Sustained intermittent regimes have not been identified as such before the mid-2000s, when Tsukahara [17] reported large-scale coherent structures from numerics in larger numerical domains. Like their counterpart in Couette flows, these structures display obliqueness with respect to the mean flow direction and a complicated long-time dynamics. The dynamics at onset in particular have remained mysterious [18] and, although this is currently debated, could follow a scenario different from the directed percolation one proposed for Couette flow. [9,19,20]. In the last years, the so-called transitional regime of plane channel flow has attracted renewed attention after new experimental studies. Whereas the works in Refs [21–23] focused on the minimal transition amplitude for spot

35 development, other studies [24–29] focused on the sustained intermittent regimes and their statistical
 36 quantification.

37
 38 Experimentally the finite length of the channel sets a limitation to most statistical approaches.
 39 Numerical simulation in large domains combined with periodic boundary conditions is a
 40 well-established way to overcome such limitations. Surprisingly, despite a large number of numerical
 41 studies of transitional channel flow, investigation of spatiotemporal intermittency in large enough
 42 domains has not been possible before the availability of massive computational resources. Owing to
 43 recent numerical studies [30–32], there is currently a good consensus about a few facts concerning
 44 the transitional regime : laminar-turbulent bands with competing orientations emerge progressively
 45 as the Reynolds number is reduced below $Re_\tau \approx 100$, and their mean wavelength increases as the
 46 Reynolds number is decreased. At even lower flow rate the bands turn into isolated spots with a
 47 ballistic dynamics rather than forming a seemingly robust stripe pattern [33–35]. The global centerline
 48 Reynolds number for the disappearance of the stripes is close to 660 [18,27]. However many questions
 49 remain open. The most sensible theoretical issues revolve around the (still open) question of the
 50 universality class of the transition process (see Ref. [18]), the role of the large-scale flows [23,25,36,37]
 51 in the sustainment of the stripes, or the mutual way different stripes interact together.

52
 53 There is also a lack of quantitative data about the patterning regime itself. The present
 54 special issue is an opportunity to document the geometric characteristics of the stripe patterns in
 55 unconstrained settings. Moreover, there is an ongoing philosophical question about whether traces
 56 of spatiotemporal intermittency can be found in the fully turbulent regimes commonly reported at
 57 higher Reynolds numbers. In the present paper, using numerical simulation in large domains, we
 58 focus on three specific points hitherto undocumented : the angular distribution of turbulent stripes,
 59 the statistics of the laminar gaps between them, and high-order statistics of the local and instantaneous
 60 bulk velocity, wall shear stress and turbulent kinetic energy. The outline of the paper is as follows
 61 : Section 2 introduces the numerical methodology with the relevant definitions. The geometrical
 62 statistics of the stripe angles are presented in section 3.1. The statistics of a few global quantities are
 63 presented in subsections 3.2, 3.3 and 3.4. A discussion of the results is made in section 4 with the
 64 conclusions and outlooks in section 5.

65 66 2. Materials and Methods

67 The present section is devoted to the methodology used for the numerical simulation of
 68 pressure-driven plane channel flow. The flow is governed by the incompressible Navier Stokes
 69 equations. Channel flow is described here using the Cartesian coordinates x, y, z , respectively the
 70 streamwise, wall-normal and spanwise coordinates. The velocity field $\mathbf{u}(x, y, z, t)$ is decomposed into
 71 the steady laminar base flow solution $\mathbf{U}(y) = (U_x, 0, 0)$ and a perturbation field $\mathbf{u}'(x, y, z, t)$. Similarly,
 72 the pressure field is decomposed as $p(x, y, z, t) = xG + p'(x, y, z, t)$. The equation governing the steady
 73 base flow for an incompressible fluid with constant density ρ and kinematic viscosity ν is given by

$$\nu \frac{\partial^2 U_x}{\partial y^2} = \frac{1}{\rho} G \quad (1)$$

74 with G a constant. Together with the no-slip condition at the walls Equation 1 yields the analytic
 75 Poiseuille solution $U_x \propto 1 - (y/h)^2$. The equation governing the perturbation field involves the base
 76 flow and reads

$$\frac{\partial \mathbf{u}'}{\partial t} + \mathbf{u}' \cdot \nabla \mathbf{u}' + \mathbf{U} \cdot \nabla \mathbf{u}' + \mathbf{u}' \cdot \nabla \mathbf{U} = -\frac{1}{\rho} \nabla p' + \nu \nabla^2 \mathbf{u}' \quad (2)$$

77 The channel geometry is formally infinitely extended, yet in the numerical representation it is
 78 given by its extent $L_x \times 2h \times L_z$ as in Figure 1, with stationary walls at $y = \pm h$ and periodic boundary
 79 conditions in x and z .

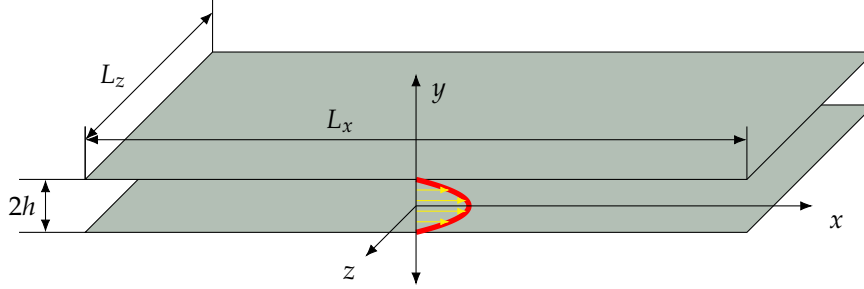


Figure 1. Schematic of the numerical domain with the laminar base flow profile (red)

80 The flow is driven by the imposed pressure gradient G assumed negative. The spanwise pressure
 81 gradient is explicitly constrained to be null. The centerline velocity u_{cl} of the laminar base profile
 82 with the same pressure gradient is chosen as the velocity scale (U) and the half gap h of the channel
 83 is chosen as the lengthscale used for non-dimensionalisation. Time is hence expressed in units of h/U .
 84 In these units the laminar velocity profile is given by $U_x^*(y_*) = 1 - y_*^2$. From Chapter 3 onwards
 85 only dimensionless quantities will be used and the $*$ notation will be dropped from there on. Primed
 86 quantities denote perturbations to the base flow while non-primed quantities involve the full velocity
 87 field, including the laminar base flow.

88
 89 In the following we shall consider, both locally and temporally fluctuating quantities, as well
 90 as their time and space averages. We denote by $\langle \bullet \rangle$ the space (x, z) average and $\bar{\bullet}$ - the time average.
 91 Space-time averages are indicated by $\langle \bar{\bullet} \rangle$. More explicitly the space average operator is defined as the
 92 discrete average over the grid points, and the time average is the discrete average sum over the total
 93 number of snapshots in the steady regime.

94
 Different velocity scales characterize the flow. One such scale is the centerline velocity u_{cl} of
 the corresponding laminar flow with the same value of G . Another one is the total streamwise flow
 through the channel, $U_b = \overline{\langle u_b \rangle}$, where

$$u_b(x, z, t) = \frac{2}{h} \int_{-h}^h u_x dy \quad (3)$$

is the so-called local bulk flow. Finally, the friction velocity is defined as $U_\tau = (\overline{\langle \tau \rangle} / \rho)^{1/2}$, where
 $\tau = (\tau_t + \tau_b) / 2 > 0$, with τ_t and τ_b the net shear stress on the top and the bottom wall, respectively
 given by :

$$\tau_{t,b}(x, z, t) = \pm \mu \left. \frac{\partial u_x}{\partial y} \right|_{t,b} \quad (4)$$

95 where $\mu = \rho\nu$ is the dynamic viscosity of the fluid. The three Reynolds numbers arising from these
 96 velocity scales are $Re_{cl} = u_{cl}h/\nu$, $Re_b = U_b h/\nu$ and $Re_\tau = U_\tau h/\nu$. For the laminar base flow they are
 97 inter-related as $Re_\tau^2 = 3Re_b = 2Re_{cl}$. Imposing a pressure gradient $G < 0$ translates into a fixed average
 98 shear stress $\overline{\langle \tau \rangle}$ on the walls which sets an imposed value of $Re_\tau = Re_\tau^c$ to stress that this is the control
 99 parameter.

100
 101 Direct numerical simulation (DNS) of Equation 2 is carried out using the open source, parallel
 102 solver called Channelflow[38,39] written in C++. It is based on a Fourier-Chebyshev discretization
 103 in space and a 3rd order semi-implicit backward difference scheme for timestepping. It makes use
 104 of the 2/3 dealiasing rule for the nonlinear terms. An influence matrix method is used to ensure

105 the no-slip boundary condition at the walls. The numerical resolution is specified in terms of
 106 spatial grid points (N_x, N_y, N_z) which translates into a maximum of $(N_x/2 + 1, N_z/2 + 1)$ Fourier
 107 wavenumbers and N_y Chebychev modes. Note that the definitions of N_x and N_z take into account
 108 the aliasing modes. The domain sizes used in this study, expressed in units of h , are $L_x = 2L_z = 250$
 109 for $55 < Re_\tau^c \leq 100$ and $L_x = 2L_z = 500$ for $39 \leq Re_\tau^c \leq 55$. The local numerical resolution used is
 110 $N_x/L_x = N_z/(2L_z) = 4.096$ and $N_y = 65$, comparable to that used in Ref. [34]. The simulation follows
 111 an "adiabatic descent": a first simulation is carried out at sufficiently high value of Re_τ^c , known to
 112 display space-filling turbulence. After the stationary turbulent regime is reached, Re_τ^c is lowered and
 113 the simulation advanced further in time. This step-by-step reduction has been performed down to
 114 $Re_\tau^c = 39$. The initial condition for the simulation is a random distribution of localized seeds of the
 115 kind described in Ref. [40]. The time required T to reach a stationary regime gradually increases as
 116 Re_τ^c is decreased. As an order of magnitude, for $Re_\tau^c = 100$, $T \approx 1500$, while for $Re_\tau^c = 50$, $T \approx 3000$.
 117 Statistics are computed, after excluding such transients, from time series of lengths up to 2×10^4 time
 118 units.

119

120 3. Results

The entire adiabatic descent is shown using a space-time diagram of the cross-flow energy shown in Fig. 2a

$$E_{cf} = \frac{1}{2} \int (u_y^2 + u_z^2) dy \quad (5)$$

121 evaluated at an arbitrary value of z (here $z = L_z/2$). The space variable is expressed in a frame moving
 122 in the streamwise direction with the mean bulk velocity $U_b(G)$ for that particular value of Re_τ^c . Since
 123 Re_τ^c is lowered over the course of time, this allows one to capture the different flow regimes preceding
 124 full relaminarisation. The intensity of turbulence, measured here by the value of E_{cf} , is seen to
 125 gradually increase as Re_τ^c is lowered. At high Re_τ^c , the so-called featureless turbulence occupies the full
 126 domain, as shown in Fig 2b at $Re_\tau^c = 100$ using isocontours of $\tau'(x, z)$. As Re_τ^c is lowered, turbulence
 127 self-organises into the recognizable pattern regime [17] shown in Fig 2c for $Re_\tau^c = 80$. As Re_τ^c is further
 128 reduced the turbulent zones become sparser (see Fig 2d for $Re_\tau^c = 60$). The spatially localized turbulent
 129 regions emerge as narrow stripes throughout the process of decreasing Re_τ^c while the gaps between
 130 them constantly increase in size. The emerging patterns never feature an array of strictly parallel
 131 stripes like in former computational approaches [19,31,41], instead they feature competing orientations
 132 as in pCf [4], see Figure 2b-d. In this regime the pattern travels with a streamwise convection velocity
 133 slightly slower than $U_b(G)$. Within the quasi-laminar gaps, E_{cf} reaches very low values, at least an
 134 order of magnitude less than in the core of the turbulent stripes. The lower Re_τ^c , the lower these values.
 135 Below $Re_\tau^c = 50$ the stripe pattern eventually breaks up to form independent turbulent bands of finite
 136 length, all parallel to each other [34], as shown in Fig 2e for $Re_\tau^c = 40$. The new resulting pattern as a
 137 whole shows negligible spanwise advection, while it propagates in x with a velocity close to $\langle \overline{u_b} \rangle$ [42].
 138 The independent turbulent bands show enhanced motility in both directions x and z . This motion
 139 relative to the frame of reference causes the tilt of the stripes seen in Fig 2a for $Re_\tau^c > 50$ as well as the
 140 apparent increase of thickness.

141 In pipe flow it was noted recently [43] that the emergence of spatial localisation does not imply
 142 the proximity to the transitional point (below which turbulence is not sustained) as long as the
 143 statistics about the size of the laminar gaps fail at displaying power-laws tails. The laminar gaps are
 144 estimated as the streamwise distance l_x between local maxima of τ (values lower than $\langle \tau \rangle + \sigma(\tau)$,
 145 with σ the standard deviation, have been discarded). The cumulative distribution (CDF) of the
 146 laminar gap size is shown in Figure 3 in lin-log coordinates. For all values of Re_τ shown, it shows an
 147 exponential tails and no algebraic part. Exponential distributions are a hallmark of spatiotemporal
 148 intermittency, unlike critical phenomena which are characterized by algebraic/power law related to
 149 the scale invariance property. The entire regime of channel flow for $39 \leq Re_\tau^c \leq 100$ can be described

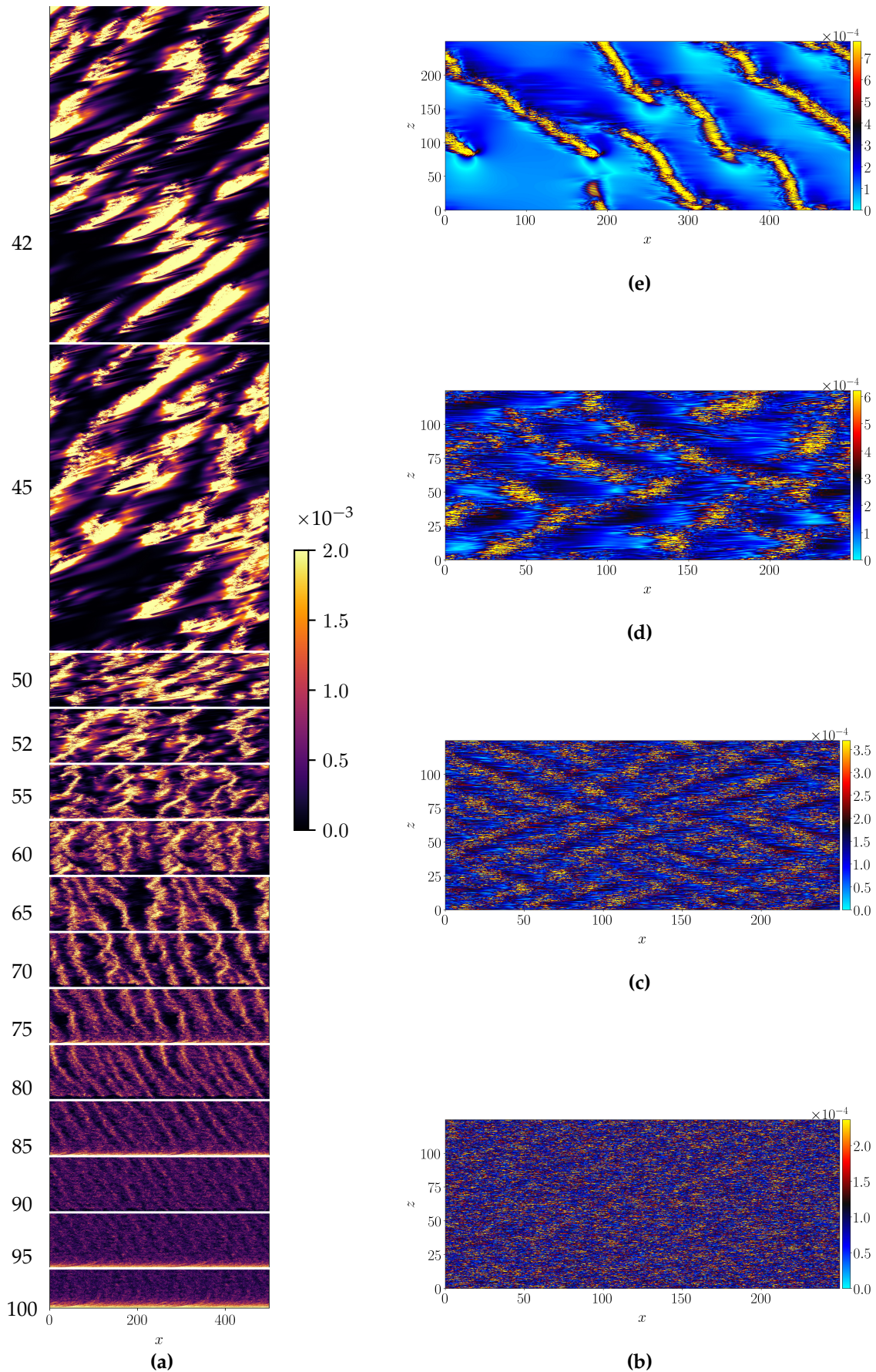


Figure 2. (a) Space-time diagram of $E_{cf}(x - U_b(G)t, t)$ for $z = L_z/2$ during the adiabatic descent protocol, in a frame travelling in the x -direction at the mean bulk velocity $\langle u_b \rangle$. Vertical axis : time with corresponding values of Re_τ^c values indicated. (b)(c)(d)(e) isocontours of $\tau'(x, z)$ for $Re_\tau^c = 100, 80, 60, 40$.

150 as being spatiotemporally intermittent, and is hence far away from any critical point. Note that the
 151 critical point of pPf is estimated to approximately $Re_{cl} = 660$ [18] i.e $Re_{\tau}^c \approx 36$ and falls outside the
 152 range of parameters investigated here.

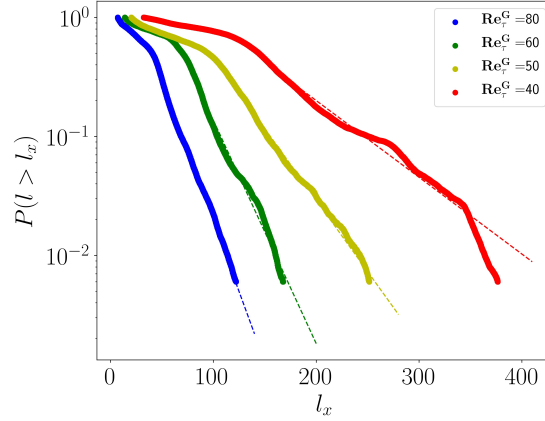


Figure 3. CDF of laminar gap size for $Re_{\tau}^c = 80, 60, 50, 40$

153 3.1. Angular Statistics of turbulent bands

The self-organization of turbulence into long band-like structures, oriented with an angle with respect to the streamwise direction, is depicted in Figure 2. The (signed) angle is computed using two different methodologies. As in Duguet *et al.* [36] in the case of pCf, the local y -integrated velocity field is found to be parallel to the bands. The same holds for pPf, as is visible in Figure 4a and Figure 4c for $Re_{\tau}^c = 60$ and 40, respectively. Note that, unlike Couette flow, pPf features advection with a non-zero mean bulk velocity. Hence the local velocity field is here computed by removing this mean advection velocity. A first estimation of the local and instantaneous band angle is therefore computed following Equation 6 :

$$\theta_L(x, z, t) = \tan^{-1} \left[\frac{\int u'_z dy - \langle \int u'_z dy \rangle}{\int u'_x dy - \langle \int u'_x dy \rangle} \right] \quad (6)$$

The second estimation is obtained from Fourier analysis and computed from Equation 7, following Ref. [44] :

$$\theta_F(t) = \tan^{-1}(\lambda_z/\lambda_x) \quad (7)$$

154 where $\lambda = 2\pi/k$, with k being the leading non-zero wavenumber identified from the power spectra
 155 (excluding the $k_x = k_z = 0$ mode). The Fourier spectrum is computed for the quantity $\tau(x, z, t)$, but
 156 similar results have been observed for other observables such as $E_{cf}(x, z, t)$ and $E_v = 1/2 \int u_y'^2 dy$. The
 157 angles can be read directly from the Fourier spectra in polar coordinates, see Figures 4b and 4d for the
 158 same values of $Re_{\tau}^c = 60$ and 40, respectively. The mean angles $\langle \overline{\theta_L} \rangle$ and $\overline{\theta_F}$ are then computed by
 159 respectively space time-averaging and time averaging the data obtained from Equation 6 and 7.

160
 161 The variation of the mean (signed) angles with Re_{τ}^c , computed using the two methods, is shown
 162 in Figure 5a, where the indices 1, 2 stand for the two band orientations. Both methods provide identical
 163 results. The variation of the (unsigned) angle of the band denoted by θ , computed as $\theta = |\overline{\theta_F}|$ is shown
 164 in Figure 5b. It is found that the mean angle θ of the bands remains approximately constant with
 165 $\theta = 25^\circ \pm 2.5^\circ$ in the range of values $60 \leq Re_{\tau}^c \leq 90$ and increases for lower value of $Re_{\tau}^c < 60$. In the
 166 patterning regime, i.e. for $Re_{\tau}^c \geq 50$, the angle of the bands is found to be distributed symmetrically
 167 with respect to zero, as a consequence of the natural symmetry $z \leftarrow -z$ of the flow. For lower Re_{τ}^c these
 168 quasi-regular patterns break down into individual localised structures analogous to individual puffs
 169 in cylindrical pipe flow. As the pattern dissolves, one single band orientation ends up dominating

170 the dynamics as shown by Shimizu and Manneville [34] for a similar domain size. The angle θ
 171 further increases as the regular pattern deteriorates, with $\theta_{max} \approx 40$ at $Re_{\tau}^G = 39$. Previous studies
 172 [18,27] have documented that the angle of the bands approach 45° close to the onset of transition.
 173 The present investigation agrees well with these studies (Figure 5b) while covering a wider range in
 174 Reynolds number, highlighting the difference between the puff regime for which $\theta \approx 40 - 45^\circ$, and the
 175 patterning regime for which θ is almost half this value (see also Fig. 2).

176

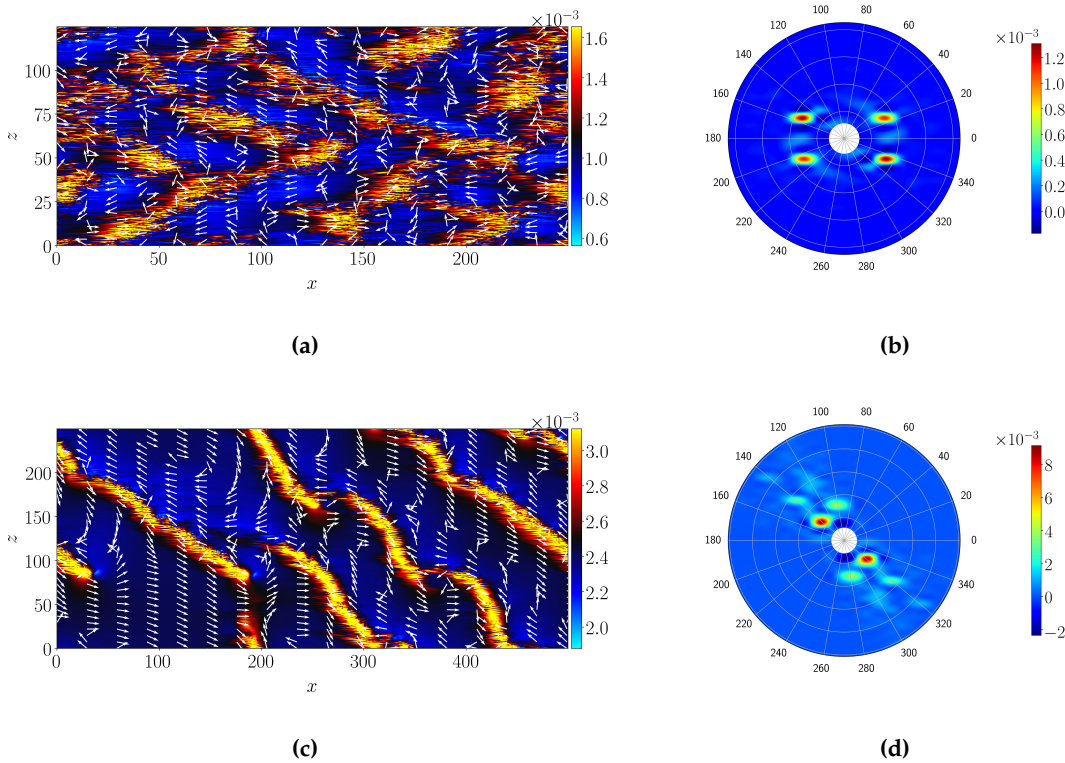


Figure 4. (a) and (c) Isocontours of τ' with the local velocity indicated by the normalized velocity vectors, at $Re_{\tau}^G = 60, 40$, respectively; (b) and (d) Instantaneous Fourier spectrum in polar coordinates for (a) and (c), respectively.

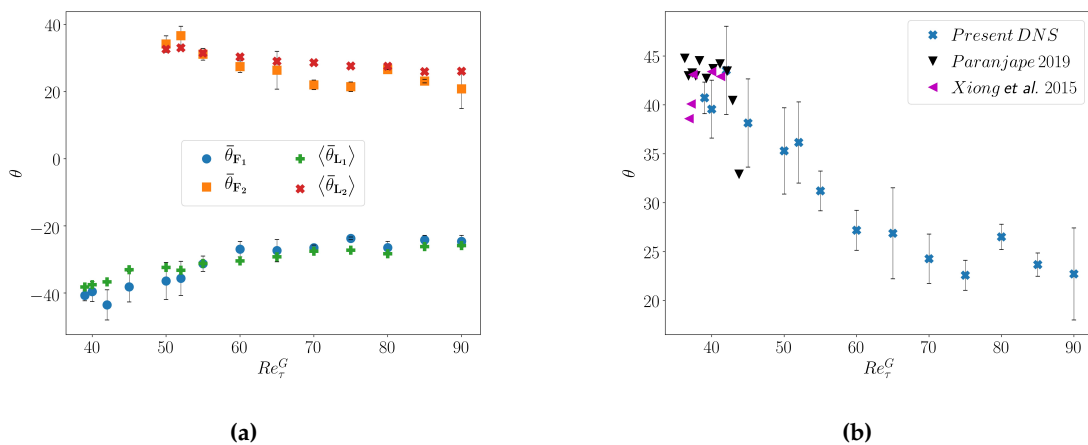


Figure 5. (a) Variation of the mean (signed) angle of the turbulent bands with Re_{τ}^G , computed from the Fourier spectra ($\bar{\theta}_{F_1}$, $\bar{\theta}_{F_2}$) and the mean (signed) angle of the local velocity ($\langle \bar{\theta}_{L_1} \rangle$, $\langle \bar{\theta}_{L_2} \rangle$) (b) Variation of the mean unsigned band angle θ along with the data from Ref. [27,30]

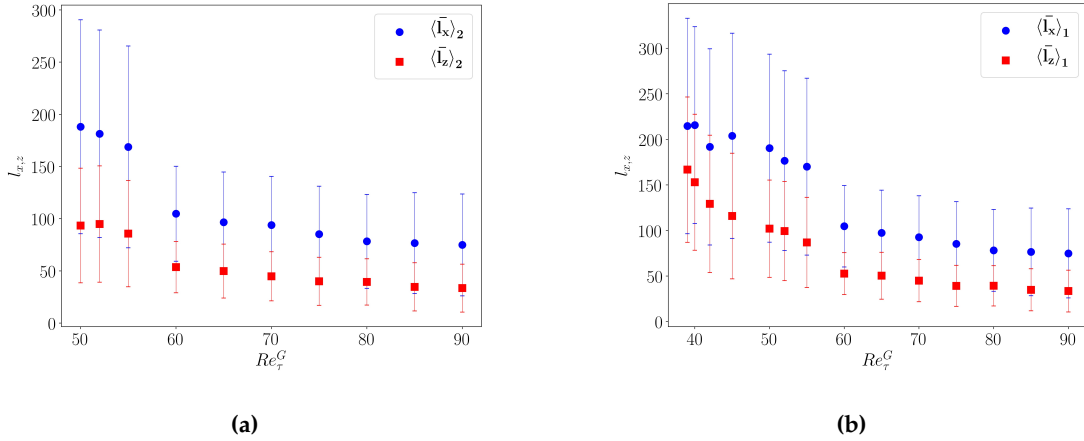


Figure 6. (a) and (b) Space-time averaged inter-stripe streamwise $\langle \overline{l_x} \rangle_{1,2}$ (blue) and spanwise $\langle \overline{l_z} \rangle_{1,2}$ (red) distances for bands of orientations 1 and 2, respectively

177 Figure 4c shows that across a band, the local large-scale velocity changes orientation [41]. This
 178 property is used to sort out the local maxima of τ (higher than $\langle \tau \rangle + \sigma(\tau)$) as belonging to one band
 179 with a particular inclination. This allows to define the respective streamwise and spanwise interstripe
 180 distances l_x and l_z between bands of the same orientation. Figure 6a,6b displays $\langle \overline{l_x} \rangle$ and $\langle \overline{l_z} \rangle$
 181 for orientations 1 and 2, respectively, as a function of Re_τ^G . Both increase when decreasing Re_τ^G . They vary
 182 in parallel in the patterning regime, hence the quasi constant angle θ of the bands. When only one
 183 band orientation survives, one observes that the increase in θ amounts to the saturation of $\langle \overline{l_x} \rangle_1$, while
 184 $\langle \overline{l_z} \rangle_1$ keeps increasing.

185 3.2. Global variables : Moody diagram

At a global level of description, the laminar and turbulent flow are traditionally represented in
 the classical Moody diagram in which the Fanning friction factor C_f defined as the ratio between the
 pressure drop along the channel length and the kinetic energy per unit volume based on the mean
 bulk velocity $U_b = \langle u_b \rangle$,

$$C_f = \frac{|\Delta p|}{1/2 \rho U_b^2} \frac{h}{L_x} = \frac{\langle \tau \rangle}{1/2 \rho U_b^2} = \frac{2 Re_\tau^G}{Re_b^2}, \quad (8)$$

186 is traditionally plotted versus Re_b as shown with plain symbols in Figure 7. For the laminar flow,
 187 the dependence of C_f vs. Re_b is analytically given by $C_{f,lam} = 6/Re_b$ (blue continuous line). In the
 188 featureless turbulent regime, it is known empirically as the Blasius' friction law scaling $\overline{Re_b}^{-1/4}$ (red
 189 continuous line). For intermediate values of Re_b , C_f clearly deviates from the turbulent branch, and
 190 remains far from the laminar value [45]. Here we notice, in agreement with [30] and [34] that $C_f \approx 0.01$
 191 remains essentially constant in this transitional regime. What is remarkable is that this regime of
 192 constant C_f coincides with the patterning regime observed for $50 \leq Re_\tau^G \leq 90$, corresponding to
 193 $690 \leq Re_b \leq 1225$, as if the respective amount of turbulent and laminar domains was precisely ensuring
 194 $C_f = cst$. As the pattern fractures, C_f increases and approaches the laminar curve. We note that the
 195 observation of this property requires large computational domains to be observed, which explains
 196 why it had not been noticed until recently, even in experiments.

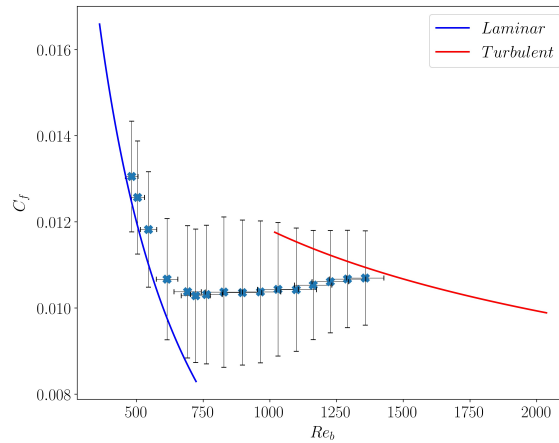


Figure 7. Friction coefficient C_f vs. Re_b , with horizontal and vertical error bars indicating the fluctuations these quantities would inherit from that of the field u_b (see text for details)

197 Given the complex spatiotemporal dynamics in the transitional regime, the bulk velocity u_b
 198 is expected to strongly fluctuate both in space and time. We also report on Figure 7, how these
 199 fluctuations would translate on Re_b and C_f , if the latter were computed using the locally fluctuating
 200 field u_b instead of its mean value U_b . These fluctuations are significant (up to 10 – 15%) and suggest to
 201 further explore them, which is the topic of the next section and the main focus of the present work.

202 3.3. Joint probability distribution of Re_τ and Re_b

203 Reynolds numbers such as Re_τ and Re_b are traditionally seen as global parameters characterizing
 204 the flow. They are defined on the basis of velocity scales obtained from space-time average. It
 205 is straightforward to extend these definitions to the local fields $Re_b(x, z, t) = u_b(x, z, t)h/\nu$ and
 206 $Re_\tau = u_\tau(x, z, t)h/\nu$, with $u_\tau(x, z, t) = (\tau(x, z, t)/\rho)^{1/2}$. Note that with this definition, $\langle Re_\tau \rangle$ is not
 207 strictly equal to the imposed Re_τ^c , because of the nonlinear relation between Re_τ and τ .

208
 209 Investigation of the entire transitional regime is provided through a two-dimensional state portrait
 210 ($Re_b - Re_\tau$) constructed from this local definition of the Reynolds number. The joint probability density
 211 distribution is constructed in this state space with the space-time data for different Re_τ^c . The state space
 212 for $Re_\tau^c = 100, 80, 60, 40$ is shown in Figure 8. The continuous blue and red lines again correspond
 213 to the scalings known analytically or empirically for the laminar and featureless turbulent flows. As
 214 expected the most probable values of Re_b and Re_τ , follow the same trend as their global counterpart :
 215 they match the continuous curve in the featureless turbulent regime, and progressively depart from
 216 it to move towards the laminar branch at the lowest Re_τ^c explored here. More interesting are the
 217 distributions. Firstly, we observe that the relative fluctuations are significantly larger for Re_τ than for
 218 Re_b , the difference being larger for the larger Re_τ^c . Secondly the distributions are not simple Gaussians.
 219 Even in the featureless turbulent regime, the marginal distribution of Re_τ is already relatively skewed
 220 (Fig. 8a₃).

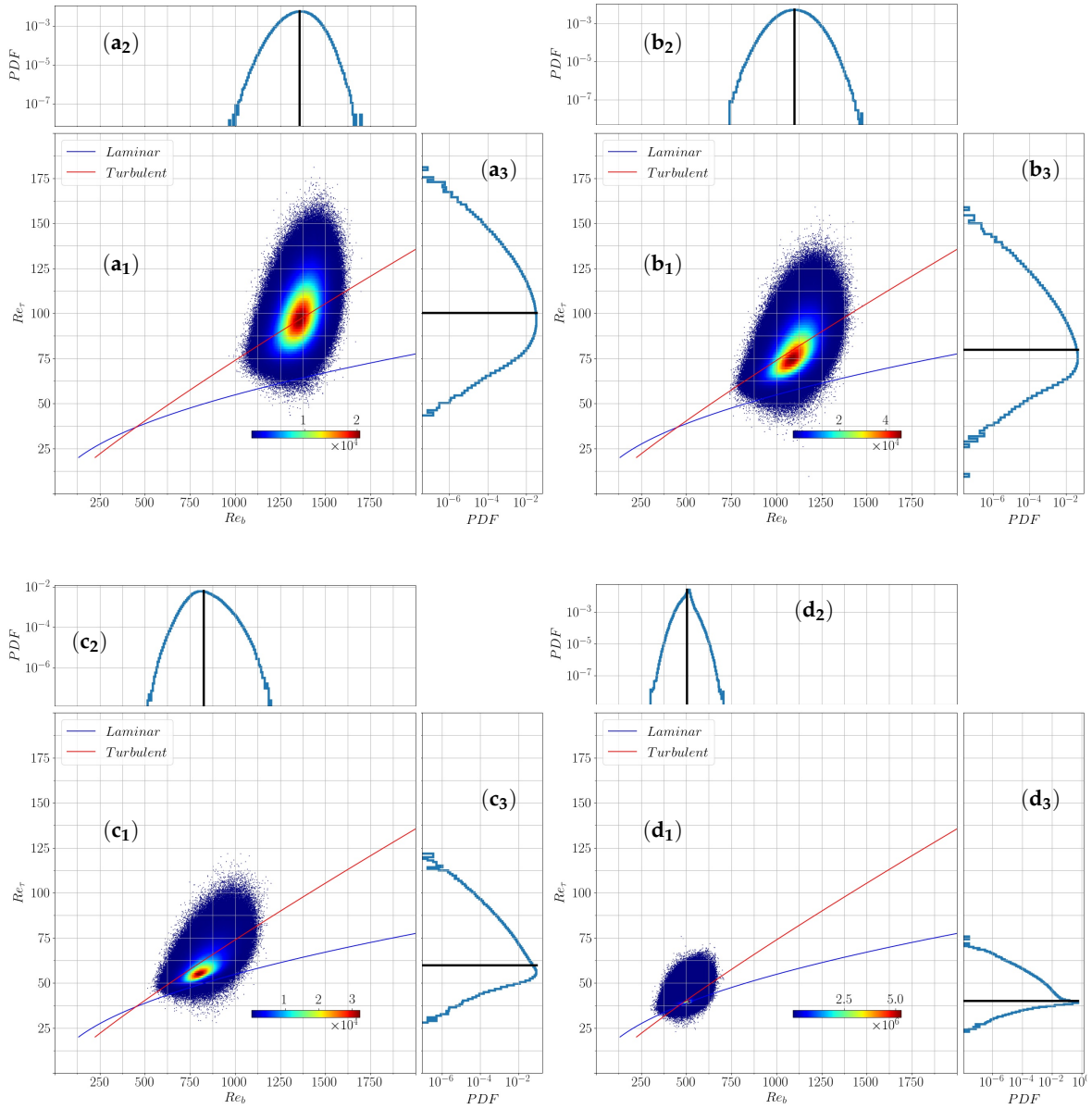


Figure 8. (a₁) (b₁) (c₁) (d₁) Joint probability distribution of the quantities Re_b and Re_τ for $Re_\tau^G = 100, 80, 60, 40$ together with their marginal distribution shown in lin-log scale for Re_b in (a₂) (b₂) (c₂) (d₂) and for Re_τ in (a₃) (b₃) (c₃) (d₃) with the mean value indicated by a vertical/horizontal black line.

221 As Re_τ^G is reduced, the overall width of the distribution decreases, but the shape of the marginal
 222 distributions of Re_τ differs more and more from a Gaussian. More specifically, although the distribution
 223 remains unimodal, we note that the marginal distribution of Re_τ is more and more skewed. We
 224 also note that the right wing of the distribution is not convex anymore. To further quantify these
 225 observations, a systematic analysis of the moments of these distribution is conducted in the next
 226 Section.

227 3.4. Higher-order statistics

228 The higher order statistics of Re_τ , Re_b and E_{cf} are presented in this section. For any field
 229 $A = A(x, z, t)$, we compute the spatio-temporal average $m = \langle A \rangle$, the variance $\sigma^2 = \langle (A - m)^2 \rangle$ and
 230 the k^{th} standardized higher order moment $\langle (A - m)^k \rangle / \sigma^k$ (for $k \geq 3$).

231

232 Their mean values of Re_b and Re_τ (Figure 9a) simply follow the trends described above for the
233 most probable value of the distribution, connecting the turbulent and the laminar branch, when
234 Re_τ^G decreases. Away from the turbulent and laminar branches Re_τ is linearly related to Re_b , in
235 agreement with the observation of a constant C_f . The standard deviation σ (Figure 9b) for Re_τ and Re_b ,
236 decrease together with Re_τ^G . This decreasing trend agrees well with the experimental wall shear stress
237 data reported in Ref. [29]. The standard deviation for E_{cf} is found to increase with decreasing Re_τ^G ,
238 matching the trend reported in Ref. [34].

239
240 The variation of the 3rd and 4th moments m_3 and m_4 , i.e. the Skewness (S) and Kurtosis (K),
241 versus Re_τ^G for the observable Re_τ and E_{cf} is shown in Figure 9c. These moments exhibit a strongly
242 increasing trend with reducing Re_τ^G for both quantities. This similarity in behavior leads to $K \propto S^2$ as
243 shown in Figure 9e. This correlation between the third and fourth statistical moments was first noted
244 in Ref. [46] for the fluctuating velocity in turbulent boundary layers at high Reynolds number. In
245 the transitional regime, the same relationship has been found to hold in the experiments of Agrawal
246 *et al.* [29] from wall shear stress data. We therefore confirm this yet-to-be-understood extension of
247 a high Reynolds number scaling down to the spatiotemporal intermittent regime. Furthermore we
248 observe that the same scaling also holds for the turbulent kinetic energy E_{cf} (Figure 9e). In contrast
249 it does not apply to Re_b (inset of Figure 9e). The reason is that, while the Kurtosis follows the same
250 trend as for the two other observables, (Figure 9d), the skewness shows a markedly different behavior:
251 it is non-monotonous, changes sign twice and exhibit a maximum in the core of the spatiotemporal
252 intermittent regime.

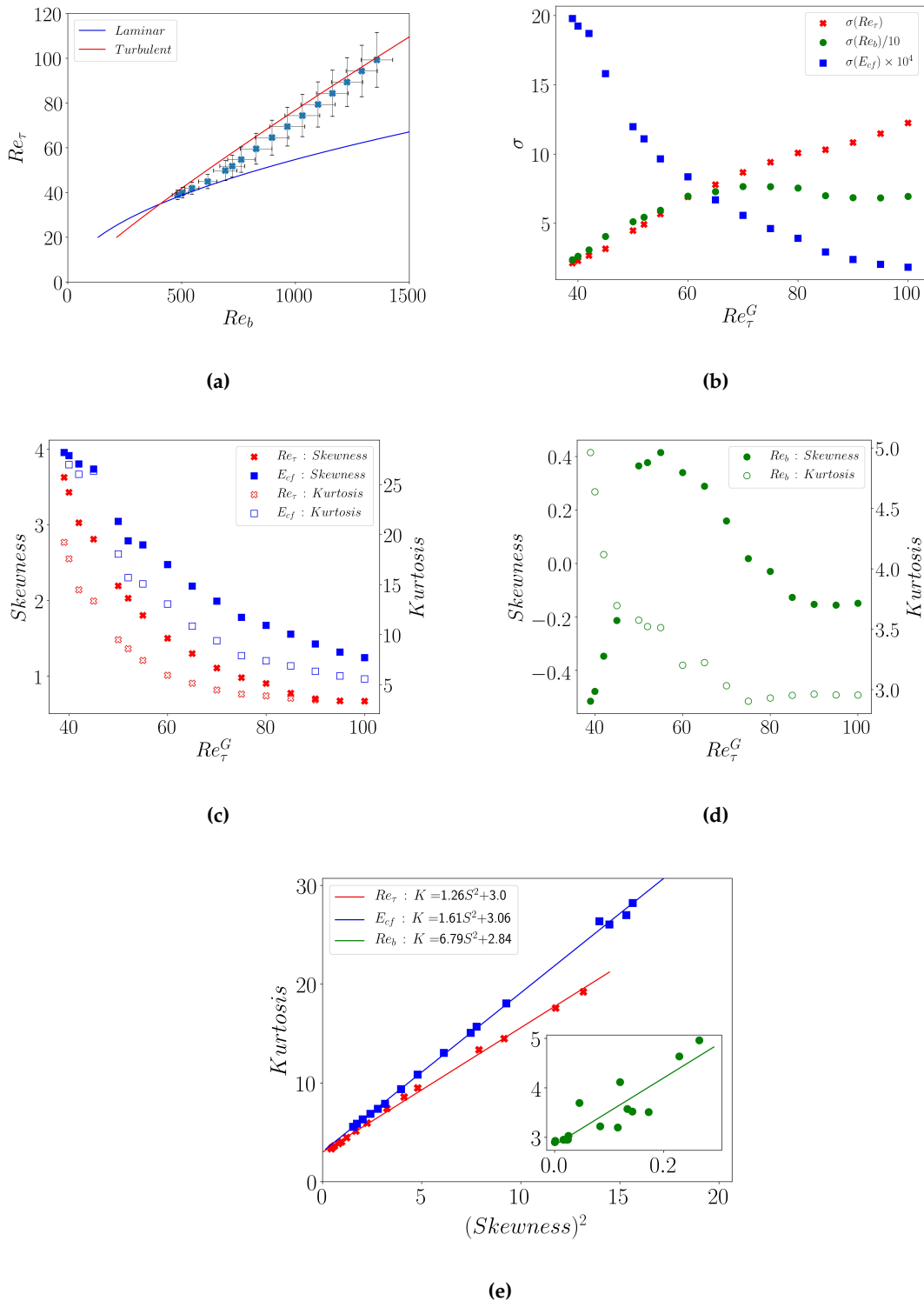


Figure 9. (a) Mean values (x_m) of Re_b and Re_τ . (b) Variation of the Standard deviation (σ) of Re_τ (red), Re_b (green), E_{cf} (blue) (indicated in the legend) vs. Re_τ^c . The $\sigma(Re_b)$ and $\sigma(Re_\tau)$ are scaled as indicated in the legend in order to make them comparable. (c) Variation of Skewness (y -axis on left, filled symbols) and kurtosis (right y -axis, open symbols) vs. Re_τ^c for the observables Re_τ (red) and E_{cf} (blue) (d) Variation of Skewness (left y -axis on the left, filled symbol) and kurtosis (y -axis on right, open symbols) vs. Re_b^c for the observable Re_b (green). (e) Kurtosis vs. squared skewness for Re_τ (red), Re_b (green, inset), E_{cf} (blue).

253 4. Discussion

254 The present simulations of the transitional regime of pPf confirm and extend previously
 255 documented knowledge, such as the constancy of C_f in the patterning regime and the variation of the
 256 band orientations close to the transition point.

257
 258 The statistical analysis of the distribution of laminar gaps reveals that the distributions are
 259 exponentially tailed over the entire parameter range $39 \leq Re_\tau^c \leq 100$, demonstrating that even the
 260 value $Re_\tau^c = 39$ remains away from any sort of critical regime, which would be marked by algebraic
 261 distributions. This is consistent with the existing estimation of the location of the transitional critical
 262 point $Re_{cl} \approx 660$ [18,27], which translates to $Re_\tau^c \approx 36$. The entire patterning regime should thus be
 263 seen as bona fide spatiotemporal intermittency, with the critical behavior and transition point being
 264 relegated to values of $Re_\tau^c < 39$. Exploring the statistics of the flow closer to the critical point would
 265 require even larger domains and longer observation times. Such an investigation is outside the scope
 266 of the current study.

267
 268 The orientation of the bands in the patterning regime for $60 \leq Re_\tau^c \leq 90$ ($1800 \leq Re_{cl} \leq 4050$) is
 269 essentially constant, with an angle $\theta = 25^\circ \pm 2.5^\circ$. This validates the choice of $\theta = 24^\circ$ as a suitable
 270 value in the numerical approach of Tuckerman *et al.* [5,31,32], where slender computational domains
 271 are tilted at a chosen value of the angle. However, this angle of 24° no longer fits the mean orientation
 272 of the independent turbulent bands in the lower range $Re_\tau^c \leq 60$ ($Re_{cl} \leq 1800$), where the orientation
 273 of the bands increases by a factor close to two, with $\theta \approx 40^\circ$ for $Re_\tau^c = 39$.

274
 275 We confirm the observation of a constant C_f in the patterning regime, which also implies
 276 $\overline{\langle Re_\tau \rangle} \sim \overline{\langle Re_b \rangle}$, as reflected in Figure 9a. This constant value of C_f in the transitional regimes further
 277 enforces the long lasting analogy with first order phase transitions [47], for which the thermodynamic
 278 parameter conjugated to the order parameter remains constant while the system evolves from one
 279 homogeneous phase to the other, when a suitable control parameter is varied. At the mean-field level,
 280 a trademark of phase coexistence, is then the presence of a bimodal distribution of the order parameter
 281 in the coexistence regime. Capturing this bi-modality is however known as being a challenge, even in
 282 simulations of standard equilibrium systems : firstly not all protocols allow for observing the phase
 283 coexistence; secondly the order parameter must be coarse-grained on appropriate length-scales as
 284 compared to the correlation lengths such that non-mean field effect do not dominate [48]. More than
 285 often, the bi-modality of the order parameter distribution is replaced by a mere concavity and a large
 286 kurtosis. If the two phases have very different fluctuations, as is the case here, one also expects a
 287 strong skewness of the distribution. Our observations extend the analogy, already reported at the
 288 level of the mean observable, to their fluctuations. However a lot remain to be done in order to
 289 further exploit this analogy, in particular by making more precise what the relevant order and control
 290 parameters are. Let us stress that whether the analogy with a first order transition is valid or not, it
 291 does not preclude the dynamics at the spinodals from obeying a critical scenario, such as directed
 292 percolation close to the laminar phase spinodal [49] and a modulated instability of the turbulent flow
 293 close to the turbulent one [4].

294
 295 Finally, the statistical moments showcased here demonstrate a correlation between the skewness
 296 and the kurtosis of both Re_τ and E_{cf} . Such a correlation, observed in both the transitional regime
 297 and higher Reynolds number turbulence but originally developed for the latter only [46], suggests a
 298 universal turbulent character, beyond the mere distinction transitional/featureless.

299 5. Conclusions

300 The transitional regime of pPf has been investigated numerically in large periodic domains. The
 301 transitional regime is composed of two sub-regimes each demarcated by a distinct behaviour. The

302 *patterning regime* is characterised, for $50 \leq Re_{\tau}^c \leq 90$, by a constant value of $C_f \approx 0.01$ and by a
 303 propagation downstream at approximately the mean bulk velocity $\langle u_b \rangle$. For lower Re_{τ}^c all the way
 304 down to the critical point close to $Re_{\tau}^c \leq 36$, independent turbulent bands define a regime analogous
 305 to the puff regime of cylindrical pipe flow. The patterns are shown to exhibit a near constant angle of
 306 inclination $\theta = 25^{\circ} \pm 2.5^{\circ}$ for $60 \leq Re_{\tau}^c \leq 90$, which increases with reducing Re_{τ}^c . Both sub-regimes can
 307 be classified as spatiotemporally intermittent, as evidenced by the exponential tails of the distribution
 308 of laminar gaps. The statistics of the local fields τ and u_b reinforce the feeling that a fruitful analogy
 309 with first order phase transitions could be developed, but the later remains to be made more precise
 310 and exploited.

311 **Author Contributions:** Conceptualization, Y.D. and O.D.; methodology, P.K., Y.D. and O.D.; data curation, P.K.;
 312 original draft preparation, Y.D. and P.K.; visualization, P.K.; supervision, Y.D. and O.D.

313 **Funding:** This research received no external funding

314 **Acknowledgments:** This study was made possible using computational resources from IDRIS (Institut du
 315 Développement et des Ressources en Informatique Scientifique) and the support of its staff. We would like to
 316 acknowledge and thank the entire team of *channelflow.ch* for building the code and making it open source. The
 317 authors would also like to thank Takahiro Tsukahara, Kazuki Takeda, Jalel Chergui, Florian Reetz, Rob Poole,
 318 Rishav Agrawal, Laurette S. Tuckerman, and Sebastian Gomé for valuable discussions and technical input.

319 **Conflicts of Interest:** The authors declare no conflict of interest

320

- 321 1. Reynolds, O. III. An experimental investigation of the circumstances which determine whether the motion
 322 of water shall be direct or sinuous, and of the law of resistance in parallel channels. *Proceedings of the royal*
 323 *society of London* **1883**, *35*, 84–99.
- 324 2. Tuckerman, L.S.; Chantry, M.; Barkley, D. Patterns in Wall-Bounded Shear Flows. *Annual Review of Fluid*
 325 *Mechanics* **2020**, *52*.
- 326 3. Coles, D. Transition in circular Couette flow. *Journal of Fluid Mechanics* **1965**, *21*, 385–425.
- 327 4. Prigent, A.; Grégoire, G.; Chaté, H.; Dauchot, O.; van Saarloos, W. Large-scale finite-wavelength modulation
 328 within turbulent shear flows. *Physical review letters* **2002**, *89*, 014501.
- 329 5. Barkley, D.; Tuckerman, L.S. Computational study of turbulent laminar patterns in Couette flow. *Physical*
 330 *review letters* **2005**, *94*, 014502.
- 331 6. Duguet, Y.; Schlatter, P.; Henningson, D.S. Formation of turbulent patterns near the onset of transition in
 332 plane Couette flow. *Journal of Fluid Mechanics* **2010**, *650*, 119–129.
- 333 7. Cros, A.; Le Gal, P. Spatiotemporal intermittency in the torsional Couette flow between a rotating and a
 334 stationary disk. *Physics of Fluids* **2002**, *14*, 3755–3765.
- 335 8. Ishida, T.; Duguet, Y.; Tsukahara, T. Transitional structures in annular Poiseuille flow depending on radius
 336 ratio. *Journal of Fluid Mechanics* **2016**, *794*.
- 337 9. Kunii, K.; Ishida, T.; Duguet, Y.; Tsukahara, T. Laminar-turbulent coexistence in annular Couette flow.
 338 *Journal of Fluid Mechanics* **2019**, *879*, 579–603.
- 339 10. Brethouwer, G.; Duguet, Y.; Schlatter, P. Turbulent-laminar coexistence in wall flows with Coriolis,
 340 buoyancy or Lorentz forces. *Journal of Fluid Mechanics* **2012**, *704*, 137.
- 341 11. Orszag, S.A. Accurate solution of the Orr–Sommerfeld stability equation. *Journal of Fluid Mechanics* **1971**,
 342 *50*, 689–703.
- 343 12. Carlson, D.R.; Widnall, S.E.; Peeters, M.F. A flow-visualization study of transition in plane Poiseuille flow.
 344 *Journal of Fluid Mechanics* **1982**, *121*, 487–505.
- 345 13. Alavyoon, F.; Henningson, D.S.; Alfredsson, P.H. Turbulent spots in plane Poiseuille flow—flow
 346 visualization. *The Physics of fluids* **1986**, *29*, 1328–1331.
- 347 14. Henningson, D.S.; Alfredsson, P.H. The wave structure of turbulent spots in plane Poiseuille flow. *Journal*
 348 *of Fluid Mechanics* **1987**, *178*, 405–421.
- 349 15. Li, F.; Widnall, S.E. Wave patterns in plane Poiseuille flow created by concentrated disturbances. *Journal of*
 350 *Fluid Mechanics* **1989**, *208*, 639–656.

- 351 16. Henningson, D.S.; Kim, J. On turbulent spots in plane Poiseuille flow. *Journal of Fluid Mechanics* **1991**,
352 228, 183–205.
- 353 17. Tsukahara, T.; Seki, Y.; Kawamura, H.; Tochio, D. DNS of turbulent channel flow at very low Reynolds
354 Numbers. TSPF Digital Library Online. Begel House Inc., 2005.
- 355 18. Tao, J.; Eckhardt, B.; Xiong, X. Extended localized structures and the onset of turbulence in channel flow.
356 *Physical Review Fluids* **2018**, *3*, 011902.
- 357 19. Lemoult, G.; Shi, L.; Avila, K.; Jalikop, S.V.; Avila, M.; Hof, B. Directed percolation phase transition to
358 sustained turbulence in Couette flow. *Nature Physics* **2016**, *12*, 254–258.
- 359 20. Chantry, M.; Tuckerman, L.S.; Barkley, D. Universal continuous transition to turbulence in a planar shear
360 flow. *Journal of Fluid Mechanics* **2017**, 824.
- 361 21. Lemoult, G.; Aider, J.L.; Wesfreid, J.E. Experimental scaling law for the subcritical transition to turbulence
362 in plane Poiseuille flow. *Physical Review E* **2012**, *85*, 025303.
- 363 22. Lemoult, G.; Aider, J.L.; Wesfreid, J.E. Turbulent spots in a channel: large-scale flow and self-sustainability.
364 *Journal of Fluid Mechanics* **2013**, 731.
- 365 23. Lemoult, G.; Gumowski, K.; Aider, J.L.; Wesfreid, J.E. Turbulent spots in channel flow: an experimental
366 study. *The European Physical Journal E* **2014**, *37*, 25.
- 367 24. Hashimoto, S.; Hasobe, A.; Tsukahara, T.; Kawaguchi, Y.; Kawamura, H. An experimental study on
368 turbulent-stripe structure in transitional channel flow. ICHMT DIGITAL LIBRARY ONLINE. Begel House
369 Inc., 2009.
- 370 25. Seki, D.; Matsubara, M. Experimental investigation of relaminarizing and transitional channel flows.
371 *Physics of Fluids* **2012**, *24*, 124102.
- 372 26. Sano, M.; Tamai, K. A universal transition to turbulence in channel flow. *Nature Physics* **2016**, *12*, 249.
- 373 27. Paranjape, C. Onset of turbulence in plane Poiseuille flow. PhD thesis, IST Austria, 2019.
- 374 28. Whalley, R.; Dennis, D.; Graham, M.; Poole, R. An experimental investigation into spatiotemporal
375 intermittencies in turbulent channel flow close to transition. *Experiments in Fluids* **2019**, *60*, 102.
- 376 29. Agrawal, R.; Ng, H.C.H.; Dennis, D.J.; Poole, R.J. Investigating channel flow using wall shear stress signals
377 at transitional Reynolds numbers. *International Journal of Heat and Fluid Flow* **2020**, *82*, 108525.
- 378 30. Xiong, X.; Tao, J.; Chen, S.; Brandt, L. Turbulent bands in plane-Poiseuille flow at moderate Reynolds
379 Numbers. *Physics of Fluids* **2015**, *27*, 041702.
- 380 31. Tuckerman, L.S.; Kreilos, T.; Schrobsdorff, H.; Schneider, T.M.; Gibson, J.F. Turbulent-laminar patterns in
381 plane Poiseuille flow. *Physics of Fluids* **2014**, *26*, 114103.
- 382 32. Gomé, S.; Tuckerman, L.S.; Barkley, D. Statistical transition to turbulence in plane channel flow. *arXiv*
383 *preprint arXiv:2002.07435* **2020**.
- 384 33. Kanazawa, T. Lifetime and Growing Process of Localized Turbulence in Plane Channel Flow. PhD thesis,
385 Osaka University, 2018. doi:10.18910/69614.
- 386 34. Shimizu, M.; Manneville, P. Bifurcations to turbulence in transitional channel flow. *Physical Review Fluids*
387 **2019**, *4*, 113903.
- 388 35. Xiao, X.; Song, B. The growth mechanism of turbulent bands in channel flow at low Reynolds numbers.
389 *Journal of Fluid Mechanics* **2020**, 883.
- 390 36. Duguet, Y.; Schlatter, P. Oblique laminar-turbulent interfaces in plane shear flows. *Physical review letters*
391 **2013**, *110*, 034502.
- 392 37. Couliou, M.; Monchaux, R. Large-scale flows in transitional plane Couette flow: a key ingredient of the
393 spot growth mechanism. *Physics of Fluids* **2015**, *27*, 034101.
- 394 38. Gibson, J.F. Channelflow: A spectral Navier-Stokes simulator in C++. Technical report, U. New Hampshire,
395 2014. Channelflow.org.
- 396 39. Gibson, J.; Reetz, F.; Azimi, S.; Ferraro, A.; Kreilos, T.; Schrobsdorff, H.; Farano, N.; Yesil, A.F.; Schütz, S.S.;
397 Culpo, M.; Schneider, T.M. Channelflow2.0. *manuscript in preparation* **2020**.
- 398 40. Lundbladh, A.; Johansson, A.V. Direct simulation of turbulent spots in plane Couette flow. *Journal of Fluid*
399 *Mechanics* **1991**, *229*, 499–516.
- 400 41. Paranjape, C.S.; Duguet, Y.; Hof, B. Oblique stripe solutions of channel flow. *Journal of Fluid Mechanics*
401 **2020**, 897.
- 402 42. Fukudome, K.; Iida, O. Large-scale flow structure in turbulent Poiseuille flows at low-Reynolds Numbers.
403 *Journal of Fluid Science and Technology* **2012**, *7*, 181–195.

- 404 43. Vasudevan, M.; Hof, B. The critical point of the transition to turbulence in pipe flow. *Journal of Fluid*
405 *Mechanics* **2018**, 839.
- 406 44. Barkley, D.; Tuckerman, L.S. Mean flow of turbulent–laminar patterns in plane Couette flow. *Journal of*
407 *Fluid Mechanics* **2007**, 576, 109–137.
- 408 45. Dean, R.B. Reynolds number dependence of skin friction and other bulk flow variables in two-dimensional
409 rectangular duct flow **1978**.
- 410 46. Jovanović, J.; Durst, F.; Johansson, T.G. Statistical analysis of the dynamic equations for higher-order
411 moments in turbulent wall bounded flows. *Physics of Fluids A: Fluid Dynamics* **1993**, 5, 2886–2900.
412 doi:10.1063/1.858698.
- 413 47. Pomeau, Y. Front motion, metastability and subcritical bifurcations in hydrodynamics. *Physica D: Nonlinear*
414 *Phenomena* **1986**, 23, 3–11.
- 415 48. Binder, K.; Landau, D.P. Finite-size scaling at first-order phase transitions. *Phys. Rev. B* **1984**, 30, 1477–1485.
416 doi:10.1103/PhysRevB.30.1477.
- 417 49. Barkley, D. Theoretical perspective on the route to turbulence in a pipe. *J. Fluid Mech* **2016**, 803.

418 © 2020 by the authors. Submitted to *Entropy* for possible open access publication under the terms and conditions
419 of the Creative Commons Attribution (CC BY) license (<http://creativecommons.org/licenses/by/4.0/>).